How to reveal subsurface defects in Kevlar® composite materials after an impact loading using infrared vision and optical NDT techniques?

A. Bendada[a], S. Sfarra[b*], M. Genest[c], D. Paoletti[b], S. Rott[a], E. Talmy[a], C. Ibarra-Castanedo[a] and X. Maldague[a]

[a] Computer Vision and Systems Laboratory, Department of Electrical and Computer Engineering, Laval University, Quebec City, G1K 7P4, Canada, Bendada@gel.ulaval.ca

[b] Las.E.R. Laboratory, Department of Industrial and Information Engineering and Economics (DIIIE), University of L'Aquila, I-67100, Monteluco di Roio, L'Aquila (AQ), Italy, stefano.sfarra@univaq.it

[c] Institute for Aerospace Research (IAR), National Research Council Canada (NRC), 1200 Montreal Road, Bldg. M-14, Room 130, Ottawa, ON, K1A 0R6, Canada, Marc.Genest@nrc-cnrc.gc.ca

*corresponding author; work telephone number: +39 0862 434336

ABSTRACT

An integrated system between infrared vision and optical non-destructive testing techniques can be considered a viable, robust and reliable approach for both aerospace manufacturing and in-service inspections. In this paper, infrared vision is applied in different spectral bands on two impacted panels made of aramid-phenolic composite by applying two different methods, respectively: (1) near and short-wave infrared reflectography and transmittography, and (2) mid-wave active infrared thermography. Furthermore, optical methods, namely digital speckle photography and holographic interferometry, are used as well to highlight the damages due to the impacts on the samples. Some techniques provide more straightforward detection capabilities than others for different defect types.

KEYWORDS

Composites; debonding; infrared vision; optical testing; defects.

1. INTRODUCTION

In the life of a structure, impacts by foreign objects can be expected to occur during manufacturing, service, and maintenance operations. In composite structures, impacts create internal damage that often cannot be detected by visual inspection. This internal damage can cause severe reductions in strength and can grow under load. Therefore, proper measures should be taken in the design process to account for these expected events. Concerns about the effect of impacts on the performance of composite structures have been a limiting factor in the wide spread use of composite materials. For this reasons, the problem of impact has received considerable attention in the literature [1].

Non-Destructive Testing (NDT) techniques are currently used to verify integrity of structural components in case of special events, and to assess and monitoring quality and effectiveness of repairs.

Infrared vision is an interesting approach that has the advantages of being non-contact, fast, and relatively inexpensive [2]. After the mid-wave infrared (MWIR) thermography (IRT) acquisitions by pulse thermography (PT) configuration, advanced signal processing techniques such as principal component thermography (PCT), pulse phase thermography (PPT), and high order statistics thermography (HOST) can be used in order to improve surface and sub-surface damage detection [3].

In the NDT field, Near-InfraRed (NIR) and Short-Wave (SWIR) reflectography and transmittography techniques can be considered a new line of research when applied on semi-transparent composite materials. Relevant publications can be found in the

literature [4], where light-emitting diodes (LEDs) working at different wavelengths are employed together with band-pass filters mounted on the camera.

The same considerations can be made for other fields (i.e., biological [5], geological [6], and art [7] fields), where the use of a microscope instead of a camera is needed for the experiments. In the latter case [7], the combination of reflectographic and transmittographic images is a well-known method.

In the present study, focused on two impacted panels made of aramid-phenolic composites, IRT in the MWIR has shown interesting complementarities when combined with NIR/SWIR reflectography/transmittography.

SWIR reflectography presents a good indication about the degree of the damaged area at the surface, whilst NIR transmittography provides information about the internal damage and fibre distribution. A comparison between images affected or not by fixed-pattern noise (FPN) is also reported in the experimental results Section.

Finally, holographic interferometry (HI) in the double-exposure (DE) version is very useful for crack detection providing complementary information to transmittography and IRT, as well as digital speckle photography (DSP) identifies the impacted area and visualizes the fibers distribution with a good correlation to NIR transmittograms. Although the impact mechanism is not the central objective of the present research, the main properties about the Kevlar® fiber are reported in Section **3**, since this information is useful for the Readers in order to better understand the NDT experimental results reported in Section **4**.

Therefore, NIR, IRT, DSP and HI results relative to the samples are presented to illustrate the promising approach of this combined assessment.

The paper is divided into three main parts. The first one is devoted to provide the Readers with relevant theoretical background about the NDT methods used along with the experimental setups; the second one explains the chemical-physical-mechanical characteristics of the Kevlar® fibers; the last one summarizes the main findings.

2. NON-DESTRUCTIVE TESTING (NDT) METHODS

2.1. Pulsed Thermography (PT)

Pulsed thermography (PT) is one of the most popular thermal stimulation methods in active thermography [8]. One reason for this is the quickness of the inspection relying on a short thermal stimulation pulse, with duration going from a few milliseconds for high conductivity material inspection (such as metal) to a few seconds for low conductivity specimens (such as plastics).

According to the testing methodology in PT, the inspected sample surface should be heated uniformly. For this purpose, a double or multiple flash lamp system with lamps arranged symmetrically with respect to the IR camera is the preferred configuration as it permits both increase and homogenization of the excitation power density over the sample surface. Flash lamps differ concerning their heat radiation elements and their constructions. Lamps with an open air emitter need additional transparent filters. The

filter is utilized to retain the infrared radiation coming from the hot shell of the lamp emitter after the excitation. This radiation is undesirable as it can be reflected from the sample surface and surrounding objects into the camera lens, affecting the thermal image.

The maximum amount of energy that could be injected into the target has an upper limit determined by the temperature at which the material will begin to be damaged. In practice, heat deposition boundary condition is set as a radiation pulsed stimulation with pulse parameters: duration, amplitude and shape. Tossel [9] discussed the different effect of heat deposition scenarios on thermography modelling. Side walls are set adiabatic and facial nodes incorporate radiation and convection heat losses. Defectives are modelled air-gaps embedded in medium. The maximum temperature contrast developed on the surfaces of a defective sample will be a function of input pulse duration and power. These, in turn, are governed by the maximum allowable surface temperature rise and material thermal constants. It is informative to first consider the relationship between these parameters for transient heat flow in a defect-free isotropic sample. When, at time $t = 0$, a slab of material is exposed to a constant heat source q_0, per unit area of surface, it will initially behave as a semi-infinite solid. At some time, t_p, the heat flow will penetrate to the rear surface and this will modify the temperature distribution through the slab thickness. Using this thermal penetration time, the problem is solved by dividing into pre-penetration and post-penetration periods. For more information, the Readers can consult [10].

In order to detect a defect, the signal must be above the Noise Equivalent Temperature Difference (NETD), or stated in another way, the temperature signal of a defect must have a signal-to-noise ratio (SNR, n) greater than 1 [10]. It is customary to define the minimum signal detection level to be a multiple of the NETD, with a rule of thumb SNR value of $n = 2$. The temperature difference needed to detect the back side of the target [11] is given as: $\Delta T_{side} = n\sigma$, where σ = NETD. The minimum energy required for detecting the back side is given by: $Q_{min} = n\sigma\rho CL$, where ρ is the density, C is the specific heat, and L is the thickness of the layer. In order to observe a defect, the signal detection level must be an additional factor greater than the back side detection level. Thus for a given signal level, $m\sigma$, and a detectability threshold, $n\sigma$, the maximum defect depth able to be detected [11] is given by: $d_{max} = [m/(m + n)]L$, $m \geq n$. At the minimum energy level, Q_{min}, the deepest detectable defect is at a depth of $L/2$. The ability to detect deeper defects increases at a logarithmic rate with energy levels, whereas the amount of thermal energy absorbed by the target is dependent on several parameters, with a best case scenario found to have an efficiency of approximately 25%. Therefore, the flash electrical energy must be: $W_{electrical} \geq (Q_{min} \text{ x Area}) / \text{Efficiency}$, [11]. These deduction levels are for an idealized situation and represent a lower limit on energy requirements. However, the processing techniques explained in Sections **2.1.1.**, **2.1.2.**, and **2.1.3.** improve defect detection up to and beyond these limitations.

Typical thermal imagers used in PT applications are high-speed mid-IR cameras. The data collection and processing hardware usually consists of a computer to store the data and perform additional processing (Figure 1).

Fig. 1

However, some cameras include real-time processing built in the camera itself. There are several existing software packages available for processing thermal data such as the Altair-Li suite provided by Cedip, IRTools by FLIR, the ThermoFitPro software by Innovation Inc., and the open-source IR View script [12]. In this work, the PT data are analysed using the latter software, which is a Matlab© graphical user interface dedicated to IR NDT applications. It was released by the Computer Vision and Systems Laboratory (CVSL) at Laval University in Canada, as an answer to many common and current needs in IRT, among which the inspection of composite materials [13].

As mentioned, there are a great variety of processing techniques [14]. We have selected three techniques: PPT, PCT, and HOST that have shown very promising results when working with Kevlar® panels.

2.1.1. Pulsed Phase Thermography (PPT)

In pulsed phase thermography (PPT) [15], data is transformed from the time domain to the frequency domain using the one-dimensional discrete Fourier transform (DFT) [16] as is reported in Eq. (1):

$$F_n(x,y) = \Delta t \sum_{K=0}^{N-1} T(k\Delta t) exp^{(\frac{i2\pi nk}{N})} = Re_n + Im_n \quad (1)$$

where i is the imaginary number ($i^2 = -1$), n designates the frequency increment ($n = 0,1,...,N$), Δt is the sampling interval, and Re and Im are the real and the imaginary parts of the transform, respectively. Real and imaginary parts of the complex transform are used to estimate the amplitude A, and the phase ϕ, [17] as is shown in Eqs. (2) and (3).

$$A_n = \sqrt{Re_n^2 + Im_n^2} \tag{2}$$

$$\emptyset_n = tan^{-1}\left(\frac{Im_n}{Re_n}\right) \tag{3}$$

Although very useful, Eq. (1) is slow. Fortunately, the Fast Fourier Transform (FFT) algorithm is available [18] to be implemented, or can be found in the IR View software [13].

The phase, Eq. (3), is of particular interest in NDT since it is less affected than raw thermal data by environmental reflections, emissivity variations, non-uniform heating, and surface geometry and orientation. These phase characteristics are very attractive not only for qualitative inspections but also for quantitative characterization of materials.

2.1.2. Principal Component Thermography (PCT)

As is explained above, the FFT provides a valuable tool to convert the signal from the temperature-time space to a phase-frequency space, but it does so through the use of

sinusoidal basis functions, which may not be the best choice for representing transient signals, which are the temperature versus time profiles typically found in PT.

Singular value decomposition (SVD) is an alternative tool to extract spatial and temporal data from a matrix in a compact or simplified manner. Instead of relying on a basis function, SVD is an eigenvector-based transform that forms an orthonormal space. SVD is close to principal component analysis (PCA) with the difference that SVD simultaneously provides the PCAs in both row and column spaces.

The SVD of an $M \times N$ matrix $\mathbf{A}$ ($M > N$) can be calculated by $\mathbf{A} = \mathbf{URV}^{\mathbf{T}}$ [19], where $\mathbf{U}$ is a $M \times N$ orthogonal matrix, $\mathbf{R}$ is a diagonal $N \times N$ matrix (with singular values of $\mathbf{A}$ present in the diagonal), and $\mathbf{V}^{\mathbf{T}}$ is the transpose of an $N \times N$ orthogonal matrix (characteristic time). Hence, in order to apply the SVD to thermographic data, the 3D thermogram matrix representing time and spatial variations has to be reorganized as a 2D $M \times N$ matrix $\mathbf{A}$. This can be done by rearranging the thermograms for every time as columns in $\mathbf{A}$, in such a way that time variations will occur column-wise while spatial variations will occur row-wise. Under this configuration, the columns of $\mathbf{U}$ represent a set of orthogonal statistical modes known as empirical orthogonal functions (EOF) that describes spatial variations of data [20]. On the other hand, the principal components (PCs), which represent time variations, are arranged row-wise in matrix $\mathbf{V}^{\mathbf{T}}$. The first EOF will represent the most characteristic variability of the data; the second EOF will contain the second most important variability, and so on. Usually, original data can be adequately represented with only a few EOFs. Typically, a 1000 thermogram sequence can be replaced by 10 or less EOFs [3].

2.1.3. Higher Order Statistics Thermography (HOST)

The most commonly employed statistic parameters are measures of central tendency and variability, with the mean and the variance being the most representative ones. Theoretically, only the first four statistic parameters have a physical definition in the mathematical study of distribution. These are the mean, variance, skewness and kurtosis, corresponding to the first, second, third and fourth statistical moments, respectively. The mean μ is the average score in a distribution; the variance σ^2 (i.e. the second central moment of a distribution) is a measure of statistical dispersions about the mean of the distribution. These two parameters can be expressed as in Eqs. (4) and (5), respectively [21]:

$$\mu = E[X] = \frac{1}{P}\sum_{n=1}^{P} X_n \tag{4}$$

$$\sigma^2 = E[(X - E[X])^2] \tag{5}$$

The standardized central moments M_I, where the superscript I indicates the moment order, can be defined as in Eq. (6):

$$M_I = \frac{E[(X - E[X]^I)]}{\sigma^I} \tag{6}$$

Skewness is the third standardized central moment (I=3), which represents a measure of symmetry, or more precisely, the lack of symmetry of a distribution. Kurtosis is the fourth moment (I=4) and characterizes the relative flatness of a distribution in relation to the shape of a normal distribution. Standardized central moments of higher-order present large values due to the high-power terms involved in their calculations, and they cannot often be defined physically. They are associated to the presence of outliers in the distribution.

In order to take advantage of HOS for active thermography, the histogram distributions of the temperature versus time profiles can be reconstructed. Histograms for pulsed thermographic thermal profiles do not have a normal distribution. All distributions are asymmetrical and skewed to the right, *i.e.* they are positively skewed and their skewness parameter has a positive value.

Nevertheless, the skewness value increases with the defect depth and is the highest value for non-defective areas. Hence, the skewness value of a data distribution obtained from the surface temperature evolution depends on both the subsurface defect presence and the defect depth [22]. It is therefore possible to obtain a HOS map, *i.e.* a single image, providing an indication about the presence or no-presence of defects and the relative depths.

2.2. Non-Thermal Infrared Vision (NIR/SWIR)

Non-thermal infrared vision is based on the detection of near (NIR, from ~0.75 to 1 μm) or short-wave (SWIR, from ~1 to 2.5 μm) infrared radiation reflected from (reflectography) or transmitted through (transmittography) the object of interest. Proper selection of a continuous and uniform active illumination source is a critical part of a non-thermal inspection system. For instance, incandescent lamps provide a wide electromagnetic (EM) spectrum, going from the ultraviolet (UV, from 0.01 to 0.35 μm) to the very long wave infrared (VLWIR, from 14 to 1000 μm). Fortunately, a vast part of the radiation from such a source is in the visible and the NIR and SWIR spectral bands. Therefore, incandescent lamps can be used as an illumination source. On the contrary, the EM spectrum of fluorescent lamps is narrower and with a few distinctive high-intensity peaks mostly in the visible spectrum. Hence, this type of illumination is less attractive for the present application.

Light-emitting diodes (LED) are an example of a very interesting illumination source since they provide a narrow spectrum at specific wavelengths, from UV to VLWIR including NIR/SWIR [23]. The radiation source can be combined with the utilization of narrow-band filters to further improve contrast. NIR offers the possibility to reveal fibres distribution, voids and porosity and subsurface defects due to impacts, and therefore this method provides information about the nature and present state of semi-transparent composite materials made by Kevlar® fibers. The NIR and SWIR parts of the radiation, which practically contain no thermal emissions, can penetrate thin layers of sample before being reflected back to the surface from a non-absorbing media, whilst

this same radiation will be absorbed by other elements such as thermosetting or thermoplastic resin. An experimental setup is shown in Figure 2.

Fig. 2

The reflectance R of a uniform layer of resin with defined thickness x can be derived from Eq. (7) [24]:

$$R = \frac{1 - R_s\left(a - b \cdot coth(bSx)\right)}{a - R_s + b \cdot coth(bSx)} \tag{7}$$

where $a = [(S+K)/S]$, $b = \sqrt{(a^2 - 1)}$, S = scattering coefficient of the resin layer; K = absorption coefficient of the resin layer and R_s = reflectance of the fiber layer. When a subsurface defect is under a resin layer, Eq. (8) can be derived:

$$R = \frac{1 - R_U\left(a - b \cdot coth(bSx)\right)}{a - R_s + b \cdot coth(bSx)} \tag{8}$$

where R_U is the reflectance of the resin.

From equations (7) and (8) it follows that infrared light reflected from a sample carries information about the resin. Optical contrast of resin image will increase if:

- thickness x of resin layer decreases;
- scattering and absorption coefficients S and K of resin layer decrease;
- difference between reflectance of fiber layer R_s and resin R_u increases.

The optimal sensitivity band of the camera for IR reflectography is up to wavelength around 2000 nm. NIR cameras are in most cases based on lead sulfide (PbS), indium gallium arsenide (InGaAs) or platinum silicide (PtSi) image sensors, in either charge-coupled devices (CCDs), or complementary metal–oxide–semiconductors (CMOS). Many resins have absorption coefficient small enough also in the band 800 - 1300 nm. Therefore, silicon CCD cameras with a 800 nm short-wavelength cut-off filter (Schott UG8) is have used. A filter is also used to suppress sensitivity of detector in the visible band. The main advantage of such a solution is, besides the relatively low price of such an equipment, the high spatial resolution of contemporary silicon CCD arrays (more than 7 millions of pixels against less than 1 million pixels for NIR/SWIR cameras at best). The camera signal is digitized by a frame-grabber, and then digitally processed by a personal computer. The resulting image can be stored and printed or displayed on a computer screen [25]. Therefore, the digital NIR/SWIR system has several advantages:

- real-time information about presence of subsurface defects;
- good quality of NIR/SWIR images due to digital image processing;
- possibility to digitally compare infrared and visible images.

2.3. Double-Exposure holographic interferometry (DE-HI)

The general principle of holographic non-destructive testing [26] is widely known: the sample under test is subjected to some kind of stressing which is uniformly distributed across its surface; the stress must be chosen in such a way that the anomalies

induce detectable perturbations in the surface deformations, i.e. a mechanical state of stress is a result of a thermal stress [26]. In continuum mechanics, stress is a measure of the internal forces acting within a deformable body. Quantitatively, it is a measure of the average force per unit area of a surface within the body on which internal forces act. The internal forces arise as a reaction to external forces applied to the body.

During the HI experiments, a thermal stress obtained by heating the surface with a lamp or a stream of warm air, is chosen empirically with guidance provided by an analysis of anticipated deformation. The interpretation of the interference pattern is briefly described next. Almost any kind of defect situated close enough to the surface acts as a stress concentrator and locally modifies the state of deformation. Using one of the well-established holographic interferometric techniques (real time, double-exposure, sandwich holography), one can then visualize the deformation state in the form of interference fringes superimposed on the object's surface. The local disturbances produced by the defects are easily identified as anomalies in the fringe pattern [27, 28]. The number and holographic appearance of detected defects depend upon the object's characteristics and the testing technique. The testing technique is characterized by a particular setup and involves a particular association between the stressing method and the interferometric technique being used.

Interested Readers can consult the double-exposure (DE) experimental setup reported in [29] and applied in this work. DE is not a dynamic technique, i.e. the information on intermediate states of the tested object is lost. However, the fringes have a very good contrast. A 500 W lamp is used for 10 s in order to produce a mechanical state of stress.

In double-exposure interferometry, one makes two successive holograms on the same film. If the object under observation deforms/displaces between the two exposures of the plate, the phase difference between light beams arriving at a specific observation point, from the object and its displaced/deformed copy, is encoded in form of fringe patterns [26]. These fringes are described by a fringe-locus function $\Delta\phi$, constant values of which define fringe-loci on the object's surface. This fringe-locus function can be related to the optical path length variation of the light. The problem is then to find the relation between the fringe-locus function and the deformation/displacement. With reference to Fig. 3a, the optical path length of the light for the object in the normal state is denoted by L_{N}:

$$L_{\mathrm{N}} = |\boldsymbol{SO}_{\mathrm{N}}| + |\boldsymbol{O}_{\mathrm{N}}\boldsymbol{H}|, \tag{9}$$

Fig. 3

where $\boldsymbol{S}$ = point of light source, $\boldsymbol{O}_{\mathrm{N}}$ = point on the surface of the object in its normal state, and $\boldsymbol{H}$ = point in the hologram plane. When the surface of the object is deformed, the point $\boldsymbol{O}_{\mathrm{N}}$ changes in $\boldsymbol{O}_{\mathrm{D}}$. With the object in the deformed configuration, the optical path length of the light, denoted by L_{D}, is:

$$L_{\mathrm{D}} = |\boldsymbol{SO}_{\mathrm{D}}| + |\boldsymbol{O}_{\mathrm{D}}\boldsymbol{H}|. \tag{10}$$

The optical path change related to the object deformation is:

$$\Delta l = L_{\mathrm{D}} - L_{\mathrm{N}}. \tag{11}$$

The path variation Δl is related to $\Delta\phi$ by $2\pi/\lambda$; therefore, the phase change can be written as:

$$\Delta\phi = \frac{2\pi}{\lambda(L_{\mathrm{D}} - L_{\mathrm{N}})}. \tag{12}$$

The latter Equation, although completely general, is not in a convenient form for numerical use. If the displacement $|\boldsymbol{O}_{\mathrm{N}}\boldsymbol{O}_{\mathrm{D}}|$ is considerably smaller than the distance between the object and the point of divergence $\boldsymbol{S}$ of the object illumination beam and of the distance between the object and the holographic plate, the illumination and viewing directions for $\boldsymbol{O}_{\mathrm{N}}$ and $\boldsymbol{O}_{\mathrm{D}}$ can be assumed to be the same.

We denote with a unit vector $\boldsymbol{n}_{\mathrm{S}}$ the direction of $\boldsymbol{SO}_{\mathrm{N}}$, and with $\boldsymbol{n}_{\mathrm{H}}$ the direction of $\boldsymbol{O}_{\mathrm{N}}\boldsymbol{H}$. Note that the image used in holographic interferometry is the virtual image. This image cannot be examined directly but can be viewed by an imaging system. The direction $\boldsymbol{O}_{\mathrm{N}}\boldsymbol{H}$ depends on the viewing point and on the form of viewing used.

If we consider Fig. 3b, the optical path change $L_{\mathrm{D}} - L_{\mathrm{N}}$ can be considered to be made up of two components, $\Delta l_{\mathrm{S}} + \Delta l_{\mathrm{H}}$. Explicitly, we have:

$$\Delta l_S = |\boldsymbol{O}_N\boldsymbol{O}_D|\cos\gamma_S = \boldsymbol{n}_S \cdot \boldsymbol{O}_N\boldsymbol{O}_D, \quad (13)$$

$$\Delta l_H = |\boldsymbol{O}_N\boldsymbol{O}_D|\cos\gamma_H = \boldsymbol{n}_H \cdot \boldsymbol{O}_N\boldsymbol{O}_D. \quad (14)$$

(The assumption that $|\boldsymbol{SO}_N| >> |\boldsymbol{O}_N\boldsymbol{O}_D|$ is equivalent to assuming that $\boldsymbol{SO}_N$ and $\boldsymbol{SO}_D$ are approximately parallel, i.e. $\boldsymbol{n}'_S \approx \boldsymbol{n}_S$. Likewise, the assumption that $|\boldsymbol{O}_N\boldsymbol{H}| >> |\boldsymbol{O}_N\boldsymbol{O}_D|$ is equivalent to assuming $\boldsymbol{n}'_H \approx \boldsymbol{n}_H$). Thus, the phase change due to the displacement $|\boldsymbol{O}_N\boldsymbol{O}_D|$ is given by:

$$\Delta\emptyset = \frac{2\pi}{\lambda}[\boldsymbol{n}_S - \boldsymbol{n}_H] \cdot \boldsymbol{O}_N\boldsymbol{O}_D. \quad (15)$$

When the point source and the point of observation are placed at finite distance from the object, the illumination and observation directions ($\boldsymbol{n}_S$ and $\boldsymbol{n}_H$) will vary across the object surface. The sensitivity (displacement per fringe) then varies across the object surface, but for small objects and reasonably long distances to the source point and the observation point, this variation will be quite small.

Because of the random phase variations across the object wave front, only waves from corresponding points on the two interfering wave fronts contribute effectively to the interference fringes. For a specific viewing direction, the phase difference $\Delta\phi$ between the waves from two points ($\boldsymbol{O}_N$, $\boldsymbol{O}_D$) is given by Eq. 15. Therefore, this phase difference will vary over the range of viewing directions defined by the aperture of the viewing lens, resulting in a loss of contrast of the fringes. However, it is possible to find

a plane in which the variation of $\Delta\phi$ is minimum over this range of viewing directions; this is the plane of localization of the fringes. The position of the plane of localization depends on the type of displacement and on the aperture of the viewing lens.

When the fringe localization plane is widely separated from the object surface, a precise identification between a point on the fringe plane and a point on the object cannot be made. For a correct interpretation of the fringe pattern, it must be localized on the object surface.

Using a sufficiently small observing aperture, i.e., a sufficiently large f-number, distinct fringes can be observed in the plane of the object, and can be related to the object surface deformation/displacement [26].

2.4. Digital Speckle Photography (DSP)

Speckle photography is a technique characterized by a relatively low complexity in the hardware. Digital Speckle Photography (DSP), sometimes referred to as Electronic Speckle Photography (ESP), is a well established technique based on the calculation of the geometrical displacement of a speckle pattern [30]. One of the key features of DSP development and success is the possibility to perform computerized image analysis. In the cross-correlation approach, sub-images are extracted from the reference image and the deformed image; then the correlation pattern is obtained using suitable correlation filters. The peak location in the correlation surface gives us the relative displacement between two sub-images.

As a rule of thumb, one can think that the sharper the correlation peak, the more reliable is the estimation of the peak position. However, this is not completely true because noise tolerance is very important. Furthermore, the coarse structure and finite size of the photosensor limit the accuracy in determining the peak position. This problem can be alleviated by sub-pixel analysis [31].

DSP is mainly used to detect in-plane displacements and their gradient components, and in this field a very simple way to perform data processing by the cross-correlation approach is given by the possibility of using existing Particle Image Velocimetry (PIV) software with only minor modifications. In the present work, pattern displacements are evaluated using correlation algorithms based on the toolbox MatPIV 1.6.1 [32]. This package has the distinctive feature of being free (Open Source) and of working in the Matlab© environment, thus sharing its capabilities of technical calculations and data visualizations. The interrogated images are divided into smaller regions, also known as sub-windows, interrogation-windows or interrogation-regions. Each sub-window in the first image is compared with the corresponding sub-window in the second image. For every possible overlap of the sub-windows, the sum of the squared difference between them is calculated looking for the position where the sub-windows are the "least unlike". Expanding the squared difference, it can be considered that only one term, the so-called cross-correlation, actually deals with both our images.

Cross-correlation is traditionally used in PIV and is the basis of many of the different algorithms performed in MatPIV since it can be calculated using FFTs and therefore can be executed faster. The functions available in MatPIV are reported in [32].

Also in the DSP measurements, a 500 W lamp is used in order to produce a mechanical state of stress, as can be seen from the experimental setup shown in Fig. 4.

Fig. 4

3. CHEMICAL-PHYSICAL-MECHANICAL CHARACTERISTICS OF THE KEVLAR® FIBERS

Kevlar®, poly-*p*-paraphenylene terephthalamite (PPTA), is an organic fiber with a distinct chemical composition of wholly aromatic polyamides (aramids). Kevlar® possesses a unique combination of high tensile strength and modulus, toughness, and thermal stability [33]. In air, PPTA demonstrates seven times the tensile strength of steel on an equal weight basis. The exceptional strength of Kevlar® fiber in tension is a direct result of its primary, secondary, and tertiary chemical structure.

When Kevlar is spun, the resulting fiber has a tensile strength of about 3.620 MPa, and a relatively density of 1.44. The polymer owes its high strength to the many inter-chain bonds. These inter-molecular hydrogen bonds form between the carbonyl groups and NH centers, i.e. the secondary chemical structure of Kevlar® as shown in Figure 5.

Fig. 5

Additional strength is derived from aromatic stacking interactions between adjacent strands.

Kevlar® also possesses a skincore morphology. The major distinction between skin and core regions is the higher degree of order and intermolecular bonding in the core region as compared to the skin. Consequently, the core region possesses an elastic modulus of 60.8 GPa. In contrast, the skin region possesses a significantly lower elastic modulus of approximately 13.4 GPa. However, the skin may be critical in the prevention of crack propagation within the crystalline core region. The tremendous behaviour of Kevlar® in tension can be attributed to structural characteristics including its stiff, extended chain conformation and nearly perfect uniaxial orientation. Despite the superlative tensile strength and modulus of PPTA in its fiber form, it possesses a comparatively low compressive strength due to its highly linear and regular microstructure. The compressive strength of Kevlar® is 1/10 of its ultimate tensile strength and it exhibits a compressive-to-tensile strength ratio of between 0.13 and 0.25, while that of carbon fiber often exceeds 1.0.

Kevlar® maintains its strength and resilience down to cryogenic (–196°C) temperatures; in fact, it is slightly stronger at low temperatures. At higher temperatures the tensile strength is immediately reduced by about 10-20%, and after some hours the strength progressively reduces further. For examples, at 160°C (320°F) about 10% reduction in strength occurs after 500 hours. At 260°C (500°F) 50% strength reduction occurs after 70 hours.

In addition to the Kevlar® used in the rubber industry, two variations of the fiber are manufactured for special application: Kevlar® 29 and Kevlar® 49. The first one is mainly used in woven ant twisted form for personnel protection, friction materials and woven fabrics and for ropes and cables. This fabric is not suitable for reinforcement purposes as the surface treatments applied are not compatible with most resin systems. The second one, has a higher modulus and is designed for reinforcement applications. Interested readers to mechanical properties of Kevlar® 49 yarns at 23°C can refer to Table 1 [34].

Mechanical property	**Value**
Tensile strength • Twisted bare yarn • Epoxy-impregnated strands	 3024 MPa 3414 MPa
Tensile elongation • Twisted bare yarn • Epoxy-impregnated strands	 2.48 % 2.62 %
Tensile modulus • Twisted bare yarns • Epoxy-impregnated strands	 121.9 GPa 130.3 GPa
Bending modulus	106 GPa
Calculated axial compression modulus	76 GPa

Theoretical PPTA crystallite tensile modulus	186 GPa
Transverse filament compressive modulus	0.76 GPa

Tab. 1 Mechanical properties of Kevlar® 49 yarns at 23°C

4. COMPARATIVE RESULTS AND DISCUSSION

In the near/shortwave infrared inspection, two cameras have been used. The first one is the Mutech© camera, operating in the near-infrared spectrum, while the second designed by Goodrich© is useful to acquire the shortwave infrared data.

Two specimens named 50B and 51B are inspected from the front side (and only in one case from the rear for comparison), both in reflection and in transmission modes. NDT data is collected after the impacts. The damages are carried out by an indentator of a determined geometry, under two different static unknown loads.

A series of defects due to the impacts arise. Some of these are not visible to the naked eye, but they are detected in the near-infrared spectrum. Transmittography, i.e. the technique for realizing the transmission mode, can be applied thanks to the Kevlar® semi-transparency in that spectrum.

Fig. 6 shows the near/shortwave infrared results from the 50B Kevlar® model. The photograph in Fig. 6a shows a slight impact indication on the front surface, whilst both the NIR reflectogram in Figs. 6b and 6d and the NIR transmittograms in Figs. 6c and 6e show more clearly the damage caused by the impact.

Fig. 6

In general, the reflectograms provide a good indication about the extent of the damaged area, while the transmittograms show information about the internal fibre distribution (some areas appear lighter than others). For reference, region of interest (ROI) is highlighted by a dotted rectangle in Fig. 6c and Fig. 6e.

Some observations can be drawn by comparing the reflectograms in Fig. 6b and Fig. 6d: (1) the concavity of the impact is more evident in the SWIR reflectogram using a 940 nm illumination source (Fig. 6d), (2) there is a non-uniform illumination in the NIR reflectogram (Fig. 6b), (3) the 940 nm source seems to provide the more uniform illumination (the geometrical disposition of the internal facets of the LED lamp is linked to a uniform illumination). The position of the source, i.e. the angle between the rays and the inspected surface, is a very important factor during the recording of digital images. In fact, specular reflection occurs when the angle of incidence and the angle of reflection relative to the normal to the surface are the same. Therefore, surface variation on the top layer will cause a corresponding variation in the presence of specular highlights, and may help to capture variations. Thus, in this method, the component is illuminated from one side only, at an oblique angle with respect to its surface. Raised surfaces facing the light are illuminated, while those facing away create shallows. This happens in Figs. 6b,d where the light angle of incidence is not the same. In the visible spectrum this method is known as raking light technique [35].

In the pulsed thermography inspection, the acquisitions has been carried out using a FLIR Phoenix Camera (3 to 5 μm). Two high-power flashes (Balcar FX 60) as heating sources are used in order to create the pulse. Advanced processing techniques are applied on the raw sequence in order to improve the defects' detectability.

In Figs. 7a-c, the defect's detection is related to the processing technique used. The PPT phasegram (Fig. 7a) and the PCT third empirical correlation function (EOF3) (Fig. 7b) seem to reveal adequately the internal fibre distribution, in agreement with the NIR transmittograms results, while the HOS 5^{th} moment reconstructed image clearly shows the impacted zone, similar to what is observed from the NIR/SWIR reflectograms in Fig. 6.

Fig. 7

On the other hand, both HI (Fig. 7d) and DSP methods (Fig. 7e) provides complementary information to IRT: the first one for cracks (dotted ellipses) and detachments (dotted circles) detection, while the second one for establishing the shape of the delaminated area linked to fibers distribution. These defects linked to the mechanical stress conditions are defined as *satellite defects* [36].

During the optical inspection, the interferograms and specklegrams are acquired using a laser having a fundamental wavelength of 532 nm, vertical polarization and a power of 250 mW. In the DSP inspection, the lamp is positioned in reflection mode, and

the same time heating and time interval (t_i = 5s) between the exposures and/or images capture are applied.

Taking into account the highly dissipative nature of the material, one frame every second is recorded in order to minimize the loss of "information-strain" between acquisitions. However, the best experimental result reported in Fig. 7e is obtained by comparing the images at 5 and 10 s after switching off the lamp. The same considerations can also be made with respect to specimen 51B. For reference, ROI is marked by a dotted rectangle in Fig. 7e.

The results inherent to the 51B sample differ from those corresponding to specimen 50B since the impact energy is different. Comparing the results of the specimens 50B (Figs. 6,7) and 51B (Fig. 8,9), we can infer that the first one had been subjected to the greatest impact.

Fig. 8

This assertion can be explained considering the presence of *satellite defects* only around the indented area of the 50B specimen, while the 51B specimen is characterized by the identification of the geometry indentator (Fig. 8c) and its horizontal delaminations (see the area surrounded by dotted rectangles in Figs. 9a-c).

In addition, the extension of the delaminated area is smaller (i.e. confined near to the impact zone) if compared to the delaminated area inherent to the 50B specimen.

Fig. 9

In this case, PCT (Fig. 8b) has not identified the fibers distribution, while the NIR transmittograms acquired on the front or on the back side (see the area marked by dotted ellipses in Fig. 8d and Fig. 9d) confirm that Kevlar® fiber-reinforced composites show poor interfacial adhesion between the Kevlar® fiber and the matrix resin, due to the low surface energy and chemically inert surface of the fibers [37]. It is interesting to note (see Fig. 6a and Fig. 8a) that, to the naked eye, there is no clear indication on which of the two specimens had been impacted with a higher energy.

Finally, it is surprising to detect the presence of a buried irregular sign, resembling a wave, by transmittography (Fig. 8d and Fig. 9d). This feature appears more clearly in Fig. 8d, which corresponds to a NIR reflectogram obtained with the Mutech© camera and an infrared cut-off filter mounted.

From these results, an explanation can now be formulated. When light strikes the specimen, it can be transmitted, reflected or absorbed. The specimen is made of molecules, and each molecule has electrons, capable of jumping to higher energy by absorbing energy. A light packet has a certain amount of energy in it according to its frequency. If this energy corresponds to one of the electron energy levels, the electron will absorb it and re-emit it as heat. The present case is focused on a semi-transparent material. These materials absorb some photons and transmit others. This will make the material look tinted (i.e., the insert wave-shaped is very dark if compared to the top

layer in Kevlar® fibers), since it only passes certain colours of light. This subsurface defect, an inclusion of foreign material, was realized during the manufacture stage.

In this case, the shape definition in term of spatial resolution grows working with a visible cut-off filter to an infrared cut-off filter mounted on the Mutech© camera. In the same way, the shape definition in term of radiometric resolution grows from the image without suppression of the FPN to the image with suppression of the FPN. The results are presented in Figure 10.

Fig. 10

FPN (also called non-uniformity) is the spatial variation in pixel output values under uniform illumination due to device and interconnect parameter variations (mismatches) across the sensor. It is fixed for a given sensor, but varies from sensor to sensor, so if v_0 is the nominal pixel output value (at uniform illumination), and the output pixel values (excluding temporal noise) from the sensor are v_{ij} for $1 \leq i \leq n$ and $1 \leq j \leq m$, then the fixed pattern noise is the set of values $\Delta v_{0ij} = v_{0ij} - v_0$. FPN consists of offset and gain components which increases with illumination, but causes more degradation in image quality at low illumination. FPN for CCD image sensors appears random; CMOS sensors (Complementary Metal-Oxide Semiconductor) have higher FPN than CCDs and suffer from column FPN, which appears as “stripes” in the image and can result in significant image quality degradation.

In Figs. 10a-c four points are surrounded by ovals. Since these signs appear also on the transmittogram of the 50B specimen (Fig. 6c), it is possible to conclude that they are related to the sensor of the camera, i.e. they are not defects of the Kevlar® specimen.

Instead, a dark spot that appears only during the acquisitions of the 51B specimen is indicated by an arrow (Fig. 10a-d), probably due to a resin-rich area. In the latter acquisitions, a wide spectrum lamp is used.

5. CONCLUSIONS

In mechanics, an impact is a high force or shock applied over a short time period when two or more bodies collide. Usually, the damages caused by an impact are inspected by an NDT technique. The combination of several NDT techniques frequently yields far more information about the defect location and extent than would result from using the same techniques separately. Similarly, knowledge of material behaviour frequently leads to confirm evidence concerning damage. The combined approach between optical and infrared NDT techniques seems very interesting and can be considered as an alternative to the standard use of ultrasound techniques for some materials.

In addition, different kind of defects are related to the manufacture stage (for example: resin-rich areas, resin-starved areas, and inclusions) and their characterization, in some cases, is very challenging. The use of transmittography technique is very pertinent in order to address this question, as well as the use of raking light

reflectography is very promising for the definition of the defect's shape. On the other hand, HI is very powerful for crack detection, as well as in order to localize the *satellite defects* due to the impacts, if combined with IRT technique.

The obtained results have led to the conclusion that, when integrated, optical and infrared vision NDT techniques provide a robust and reliable inspection system in the detection of defects after impact for bare composite materials made of Kevlar® fibers.

REFERENCES

[1] Abrate S. Impact in Composite Structures. U.K.: Cambridge University Press; 2005.

[2] Genest M, Fahr A. Thermography for non-destructive evaluation of composite structures. In: Lo J, Hoa SV, *et al* editors. Design, manufacturing and applications of composites, Proceedings of the Sixth Joint Canada-Japan Workshop on Composites, U.S.A.: DEStech Publications Inc; 2006, p. 399-406.

[3] Ibarra-Castanedo C, Piau J-M, Guilbert S, Avdelidis NP, Genest M, Bendada A, et al. Comparative study of active thermography techniques for the non-destructive evaluation of honeycomb structures. Res Nondestruct Eval 2009;20:1-31.

[4] Aoyama H, Tanaka K, Takeda N. Health monitoring technologies for fiber reinforced plastics. In: Green, *et al* editors. Nondestructive characterization of materials X, Proceedings of the 10th International Symposium on Nondestructive Characterization of Materials, U.K.: Elsevier; 2001, p. 45-52.

[5] Sivaguru M, Mander L, Fried G, Punyasena SW. Capturing the surface texture and shape of pollen: a comparison of microscopy techniques. PloS ONE 2012;7:e39129.

[6] Alley RB. Texture of polar firn for remote sensing. Ann Glaciol 1987;9:1-4.

[7] http://www-hki.fitzmuseum.cam.ac.uk/services/photo_lighting.html, accessed on November 26, 2012.

[8] Maldague X. Theory and practice of infrared technology for nondestructive testing. N.Y.: John Wiley & Sons; 2001.

[9] Tossel DA. Numerical analysis of heat input effects in thermography. J Nondestruct Eval 1987;6:101-107.

[10] Vavilov V. Pulsed thermography NDT of materials: back to the basics. Nondestr Test Eval 2007;22:177-197.

[11] Shepard S, Lhota J, Ahmed T. Flash thermography contrast model based on IR camera noise characteristics. Nondestr Test Eval 2007;22:113-126.

[12] Larsen Cory A. Document flash thermography. All graduate theses and dissertations. Paper 1018. http://digitalcommons.usu.edu/etd/1018, accessed on November 26, 2012; 2011.

[13] Klein M, Ibarra-Castanedo C, Maldague X, Bendada AH. IR-View: a straightforward graphical user interface for basic and advanced signal processing of thermographic infrared sequences. In: Vavilov VP, Burleigh DD, editors. Thermosense XXX, SPIE Defense and Security Symposium, Orlando, U.S.A, 2008, 6939: 693914.

[14] Ibarra-Castanedo C, Bendada A, Maldague X. Image signal processing techniques in pulsed thermography. GESTS Int'I Trans. Computer Science and Eng. 2005;22:89-100.

[15] Maldague X, Marinetti S. Pulse phase thermography. J Appl Phys 1996;79:2694-2698.

[16] Bracewell R. The Fourier Transform and its applications. Toronto: McGraw-Hill; 1965.

[17] Ibarra-Castanedo C, Maldague X. Pulsed phase thermography reviewed. J QIRT 2004;1:47-70.

[18] Cooley JW, Tukey JW. An algorithm for the machine calculation of complex Fourier series. Math Comp 1965;19:297-301.

[19] Rajic N. Principal component thermography for flaw contract enhancement and flaw depth characterization in composite structures. Compos Struct 2002;58:521-528.

[20] Marinetti S, Grinzato E, Bison PG, Bozzi E, Chimenti M, Pieri G, Salvetti O. Statistical analysis of IR thermographic sequences by PCA. Infr Phys Tech 2004;46:85-91.

[21] Madruga FJ, Ibarra-Castanedo C, Conde OM, Lopez-Higuera JM, Maldague XP. Infrared thermography processing based on higher-order statistics. NDT&E Int. 2010;43:661-666.0

[22] Madruga FJ, Ibarra-Castanedo C, Conde OM, Maldague XP, Lopez-Higuera JM. Enhanced contrast detection of subsurface defects by pulsed infrared thermography based on the fourth order statistic moment, kurtosis. In: Dinwiddie RB, editor. Thermosense XXXI, SPIE Defense and Security Symposium, Orlando, U.S.A, 2009, 7299: 72990U.

[23] Light-emitting diode. In *Wikipedia*: The free encyclopedia. Wikimedia foundation Inc. Encyclopedia on-line. http://en.wikipedia.org/wiki/Led, accessed on January 14, 2011.

[24] Kulbelka P, Munk F. Ein beitrag zur optic der farbanstriche. F Tech Physic 1931;12:593-601.

[25] Hain M, Bartl J, Jacko V. The use of infrared radiation in measurement and non-destructive testing. Meas Sci Rev 2005;5:10-14.

[26] Vest C. Holographic Interferometry. N.Y.: Wiley; 1979.

[27] Erf K. Holographic non-destructive testing. N.Y.: Academic Press; 1974.

[28] Borza DN. Specialized techniques in holographic non-destructive testing of composites. Comp Part B 1998;29B:497-504.

[29] Sfarra S, Ibarra-Castanedo C, Santulli C, Paoletti A, Paoletti D, Sarasini F, Bendada A, Maldague X. Falling weight impacted glass and basalt fibre woven composites inspected using non-destructive techniques. Comp Part B 2013;46:601-608.

[30] Fomin NA. Speckle photography for fluid mechanics measurements. Berlin: Springer; 1998.

[31] Sjödahl M. Digital speckle photography. In: Rastogi PK, editor. Digital speckle pattern interferometry and related techniques, Chichester: Wiley; 2000, p. 289-336.

[32] Sveen JK. The MatPIV Home. http://www.math.uio.no/~jks/matpiv, accessed on November 11, 2012.

[33] DuPont Kevlar®. Technical guide DuPont advanced fiber systems. http://www2.dupont.com/Kevlar/en_US/assets/downloads/Technical%20Guide%20for%20KEVLAR_2011.pdf, accessed on 2November 20, 2012.

[34] Stuart ML. Handbook of composite reinforcements. California: VCH Publishers, Inc; 1993.

[35] Graeme E, Martinez K, Malzbender T. Archaeological applications of polynomial texture mapping: analysis, conservation and representation. J Arch Sci 2010;37:1-11.

[36] Sfarra S, Ibarra-Castanedo C, Lambiase F, Paoletti D, Di Ilio A, Maldague X. From the experimental simulation to integrated non-destructive analysis by means of optical and infrared techniques: results compared. Meas Sci Tech 2012;23:115601.

[37] Park SJ, Seo MK, Ma TJ, Lee DR. Effect of chemical treatment of Kevlar fibers on mechanical interfacial properties of composites. J Colloid Inter Sci 2002;252:249-255.

FIGURES WITH CAPTIONS

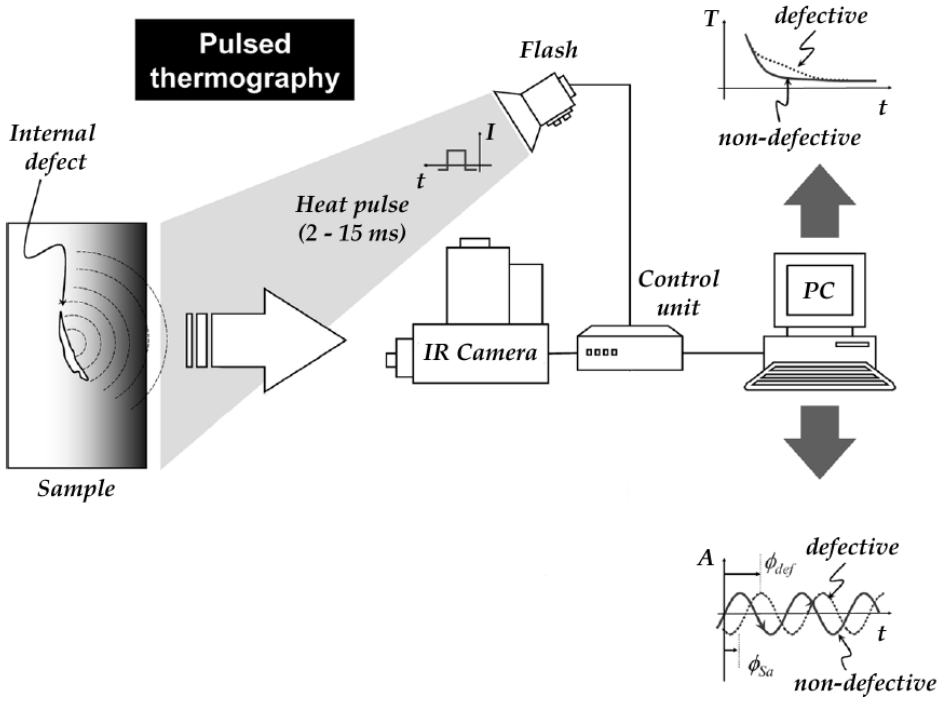

Figure 1: Pulsed thermography (PT) experimental setup.

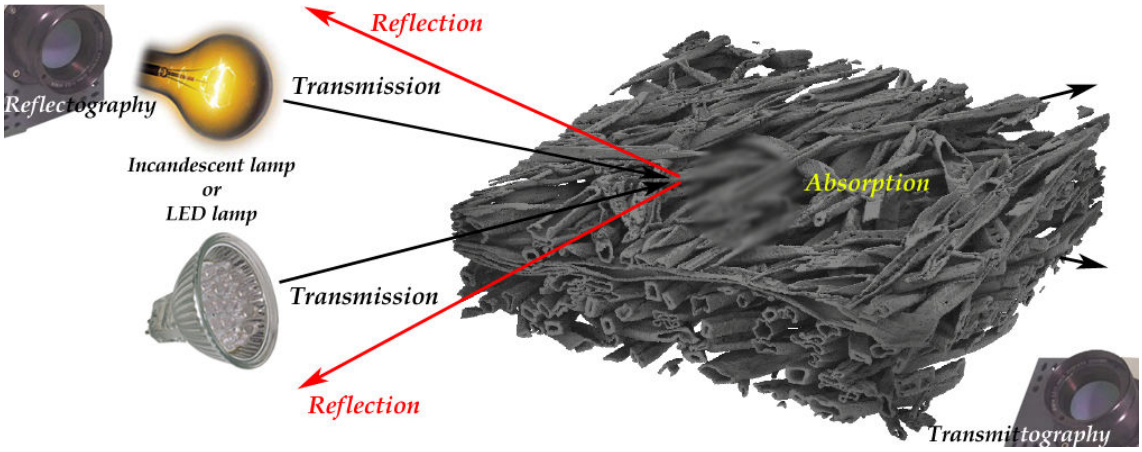

Figure 2: Reflectography and/or transmittography experimental setup.

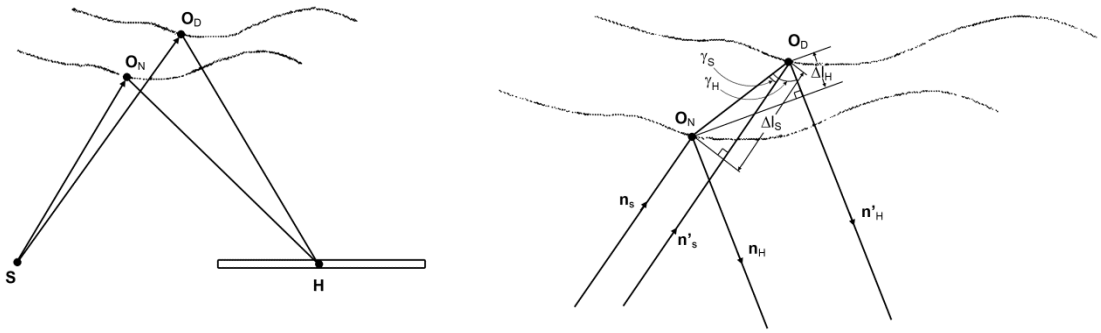

(a) (b)

Figure 3: Geometry of fringe formation for object deformation: (a) general illumination and viewing geometry; (b) the change in the optical path associated with a displacement.

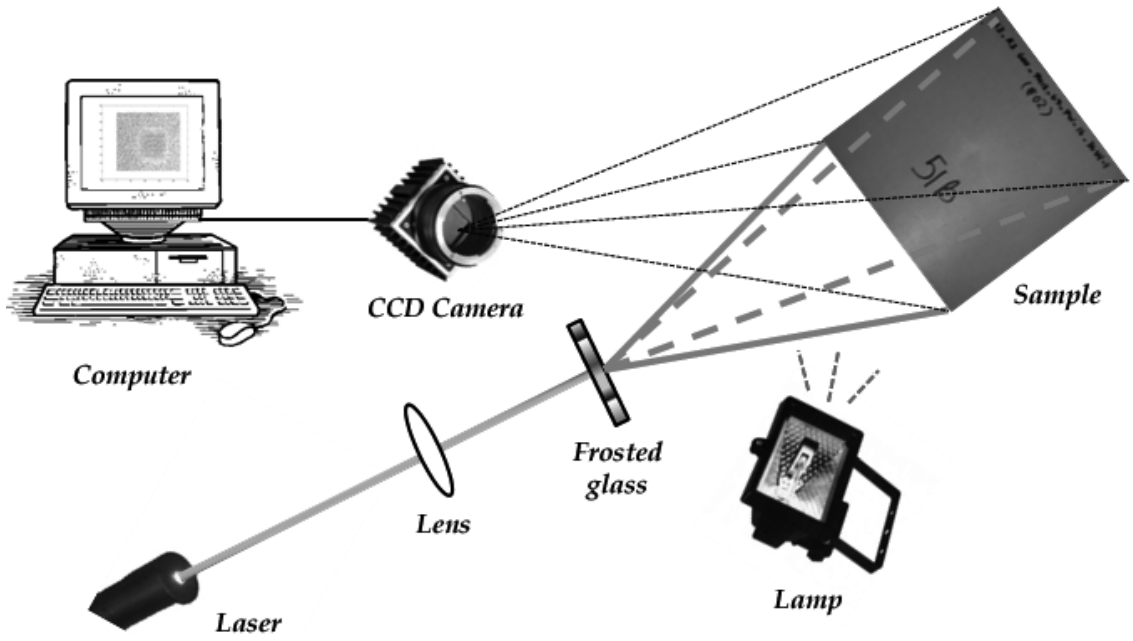

Figure 4: Digital speckle photography (DSP) experimental setup.

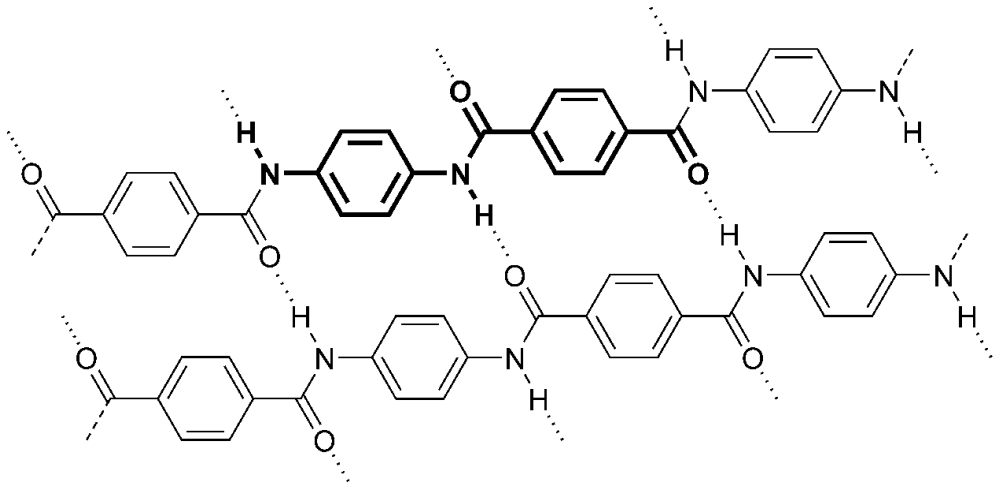

Figure 5: The secondary chemical structure of Kevlar®.

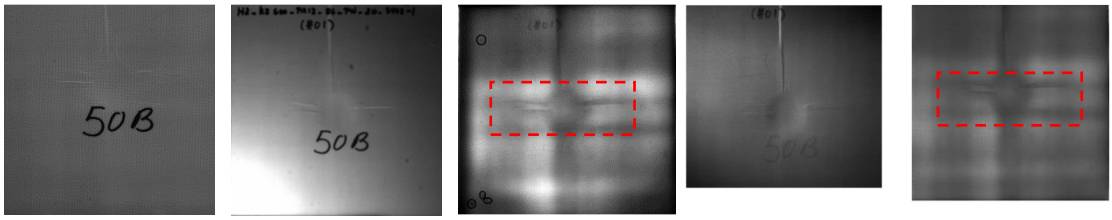

(a) (b) (c) (d) (e)

Figure 6: 50B Kevlar® impacted specimen inspected by a CCD camera. Front side: (a) photograph, (b) NIR reflectogram using a filter (Camera Mutech©), (c) NIR transmittogram using a wide spectrum source (Camera Mutech©), (d) NIR reflectogram using a 940 nm source (camera Goodrich©), (e) NIR transmittogram using a wide spectrum source (Camera Goodrich©).

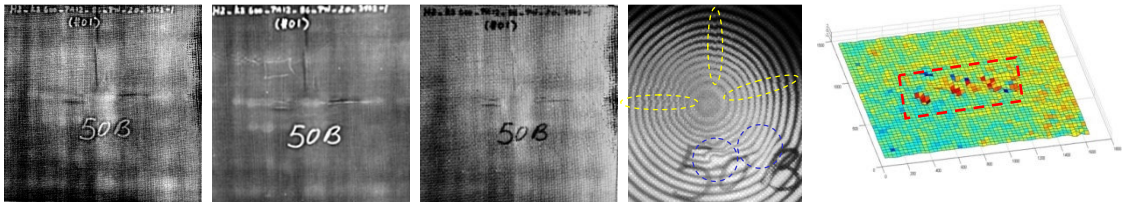

(a) (b) (c) (d) (e)

Figure 7: 50B Kevlar® impacted specimen. Front side: (a) PPT phasegram f=0.22 Hz, (b) 3rd empirical orthogonal function by PCT, (c) HOS, 5th moment reconstructed image, (d) HI-DE result (t_{exp} = 1s), (e) DSP surf result by MatPIV 1.6.1.

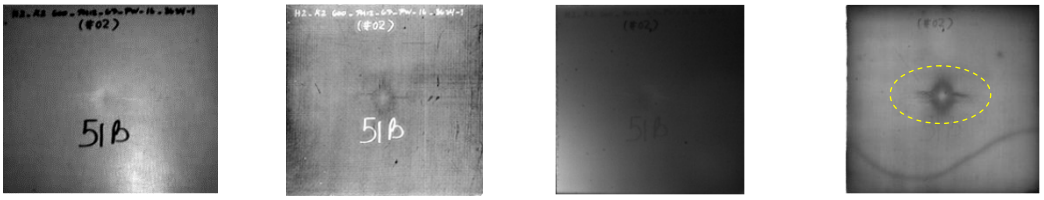

(a) (b) (c) (d)

Figure 8: 51B Kevlar® impacted specimen. Front side inspection: (a) photograph, (b) 5th empirical orthogonal function by PCT, (c) NIR reflectogram using an infrared cut-off filter (Camera Mutech©), (d) NIR transmittogram using an infrared cut-off filter (Camera Mutech©).

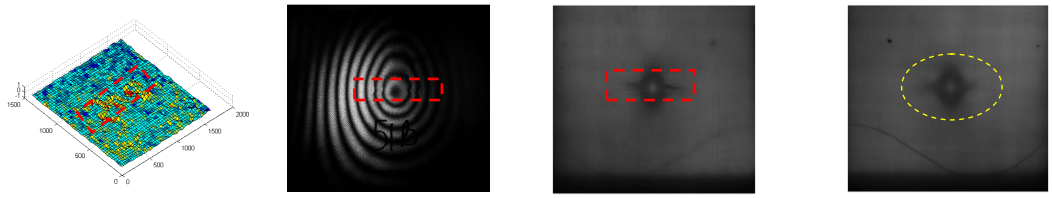

(a) (b) (c) (d)

Figure 9: 51B Kevlar® impacted specimen. Front side inspection: (a) DSP surf result using MatPIV 1.6.1, (b) HI-DE result (t_{exp} = 1s), (c) NIR transmittogram using a wide spectrum source (Camera Goodrich©), Back side inspection: (d) NIR transmittogram using a wide spectrum source (Camera Goodrich©).

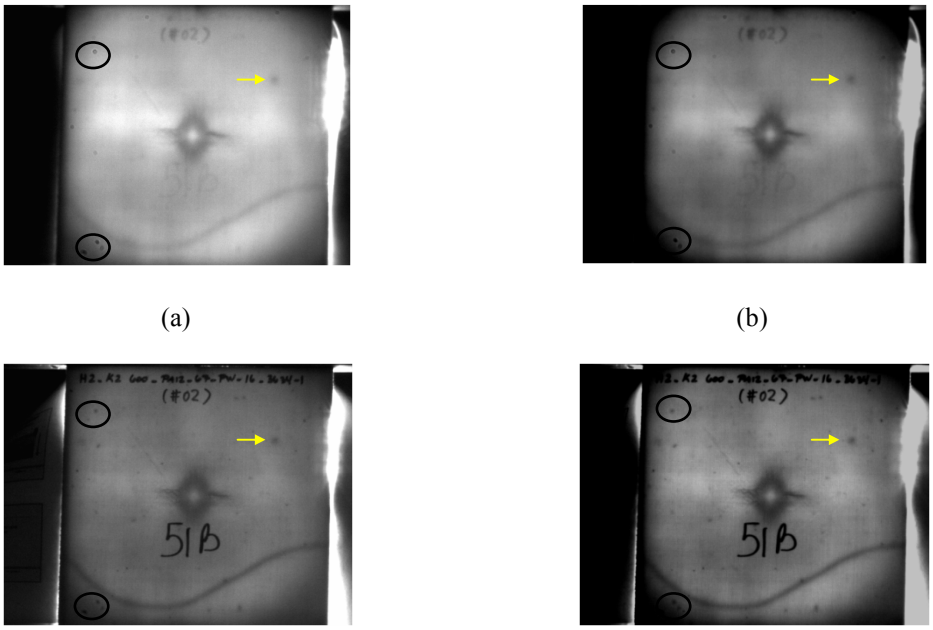

(a) (b)

(c) (d)

Figure 10: 51B Kevlar® impacted specimen. Transmittography results (Camera Mutech©). Front side inspection: (a) with a visible cut-off filter and without suppressing the FPN, (b) with a visible cut-off filter and suppressing the FPN, (c) with an infrared cut-off filter and without suppressing the FPN, (d) with an infrared cut-off filter and suppressing the FPN.